Accurate evolutions of inspiralling and magnetized neutron stars: Equal-mass binaries

Bruno Giacomazzo, Luciano Rezzolla, and Luca Baiotti

Accurate evolutions of inspiralling and magnetized neutron-stars: equal-mass binaries

Bruno Giacomazzo,[1,2,3] Luciano Rezzolla,[3,4] and Luca Baiotti[5]

[1]*Department of Astronomy, University of Maryland, College Park, MD USA*
[2]*Gravitational Astrophysics Laboratory, NASA Goddard Space Flight Center, Greenbelt, MD USA*
[3]*Max-Planck-Institut für Gravitationsphysik, Albert-Einstein-Institut, Potsdam Germany*
[4]*Department of Physics and Astronomy, Louisiana State University, Baton Rouge, LA USA*
[5]*Institute of Laser Engineering, Osaka University, Osaka Japan*

By performing new, long and numerically accurate general-relativistic simulations of magnetized, equal-mass neutron-star binaries, we investigate the role that realistic magnetic fields may have in the evolution of these systems. In particular, we study the evolution of the magnetic fields and show that they can influence the survival of the hypermassive-neutron star produced at the merger by accelerating its collapse to a black hole. We also provide evidence that even if purely poloidal initially, the magnetic fields produced in the tori surrounding the black hole have toroidal and poloidal components of equivalent strength. When estimating the possibility that magnetic fields could have an impact on the gravitational-wave signals emitted by these systems either during the inspiral or after the merger we conclude that for realistic magnetic-field strengths $B \lesssim 10^{12}$ G such effects could be detected, but only marginally, by detectors such as advanced LIGO or advanced Virgo. However, magnetically induced modifications could become detectable in the case of small-mass binaries and with the development of gravitational-wave detectors, such as the Einstein Telescope, with much higher sensitivities at frequencies larger than $\approx 2\,\mathrm{kHz}$.

I. INTRODUCTION

The use of improved and more accurate numerical techniques, together with the access to larger computational infrastructures, has brought the simulation of binary neutron-star (BNS) systems to an unprecedented level of maturity. A number of groups have reported on calculations of BNSs with different levels of approximation, for equal and unequal-mass systems, with and without magnetic fields (see, *e.g.,* [1–8] for some of the most recent works). Besides the obvious implications that these systems have in our understanding of the origin of short γ-ray bursts (GRBs), whose short rise times suggest that their central sources have to be highly relativistic objects [9], BNS systems are expected to produce signals of amplitude large enough to be relevant for Earth-based gravitational-wave (GW) detectors and to be sufficiently frequent sources to be detectable over the timescale in which the detectors are operative. Current estimates for the detection rate relative to the first-generation interferometric detectors is ~ 1 event per $\sim 40 - 300$ years, increasing to an encouraging $\sim 10 - 100$ events per year for the advanced detectors [10].

The detection of gravitational waves from neutron-star (NS) binaries will also provide a wide variety of physical information on the component stars [11]. This includes their mass, spin, and radius, which would in turn provide vital clues on the governing equation of state (EOS), and, possibly, their magnetic field. However, for this information to be extracted it is essential that accurate and long-term simulations are carried out, which span the interval ranging from the early inspiral to the decaying tail of the late ringing of the formed black hole (BH). This is indeed the goal of this work, where we focus on whether present and future GW detectors will be able to determine or not the level of magnetization of NSs. This is not an academic question as we know that NSs have very large magnetic fields and it is indeed via the magnetic-dipolar

losses that the vast majority of NSs are routinely detected as pulsars [12]. Yet, determining what the effects of magnetic fields are on the inspiral and merger of BNSs is a remarkably difficult task requiring the solution of the Einstein equations together with those of general-relativistic magnetohydrodynamics (GRMHD). So far, only three GRMHD simulations of inspiralling BNSs have been reported [3, 5, 6], and while Refs. [3, 5] considered magnetic fields that are astrophysically unrealistic[1] [13, 14], only the work in Ref. [6] has studied magnetic fields of the order of $\approx 10^{12}$ G, which are probably the strongest to be expected for NSs near the merger. Ultra-large magnetic fields are however not entirely uninteresting from a general-relativistic point of view. Indeed, as discussed in [6], the magnetic tension associated with these extremely large magnetic fields can be so strong to reduce the stellar tidal deformations during the inspiral and hence to lead to a slightly delayed time of merger.

We here present a more extended analysis than the one given in [6] and report on a systematic investigation of equal-mass BNSs systems through long-term simulations using the highest resolutions to date. The calculations cover a range of magnetic fields from $B \approx 10^8$ G up to $B \approx 10^{12}$ G, and two different masses to distinguish the phenomenology of those binaries that lead to a prompt collapse from those that lead instead to a delayed one (see the discussion in [2]). Overall, we find that magnetic fields are amplified during the merger, when the turbulent motions, triggered during the merger by the Kelvin-Helmholtz instability, curl magnetic field lines producing a strong toroidal component that reaches a strength

---

[1] We note that although NSs with magnetic fields as large as 10^{16} are widely expected to be behind the phenomenology associated with magnetars, it is unrealistic to expect that the old NSs comprising the binary have magnetic fields that are so large.

comparable to the poloidal one. The toroidal field maintains a value comparable or larger than the poloidal one during the subsequent evolution of the hypermassive neutron star (HMNS) formed after the merger. The stability of the latter, however, is influenced by the strength of the poloidal field, which can transport angular momentum outwards and trigger the collapse of the HMNS to a BH. Furthermore, equipartition among the poloidal and toroidal magnetic field components has been measured during the first 5 ms after the collapse of the HMNS, when the system consists of a rotating BH surrounded by a massive, high-density torus.

We have also analyzed in detail the GW signal emitted by these systems and found that for the timescales considered here, the overlaps in the GWs between a non-magnetized binary and a magnetized one are always above what detectors such as Advanced LIGO (advLIGO) or Advanced Virgo (advVirgo) can distinguish. Hence, it is very unlikely that present detectors will be able to measure the presence of magnetic fields. However, for sufficiently small-mass binaries, whose corresponding HMNS could survive for up to a fraction of a second (see the Appendix of [8]), the dephasing induced by the presence of magnetic fields could be measurable, especially by those detectors, such as the Einstein Telescope [15], that have higher sensitivities at frequencies larger than $\approx 2\,\mathrm{kHz}$.

The paper is organized as follows. In Section II we first summarize the formalism we adopt for the numerical solution of the Einstein and of the GRMHD equations; we then describe briefly the numerical methods we implemented in the Whisky code [16–18], we outline our mesh-refined grid setup, and we finally describe the quasi-equilibrium initial data we use. In Section III we describe the dynamics of the different models by studying both the evolution of the matter and of the magnetic field. In Section IV we instead describe the GWs emitted by these systems and we estimate the possibility to detect magnetic field effects on those signals, while in Section V we summarize our main results.

We here use a spacelike signature $(-, +, +, +)$ and a system of units in which $c = G = M_\odot = 1$ (unless explicitly shown otherwise for convenience).

II. MATHEMATICAL AND NUMERICAL SETUP

Most of the details on the mathematical and numerical setup used for producing the results presented here are discussed in depth in [6, 18–20]. In what follows, we limit ourselves to a brief overview and we describe in more details only the main differences with respect to our previous simulations.

A. Einstein and Magnetohydrodynamics equations

The evolution of the spacetime was obtained using the Ccatie code, a three-dimensional finite-differencing code

providing the solution of a conformal traceless formulation of the Einstein equations [19]. The GRMHD equations were instead solved using the Whisky code [16–18], which adopts a flux-conservative formulation of the equations as presented in [21] and high-resolution shock-capturing schemes (HRSC). The Whisky code implements several reconstruction methods, such as Total-Variation-Diminishing (TVD) methods, Essentially-Non-Oscillatory (ENO) methods [22] and the Piecewise Parabolic Method (PPM) [23]. As already discussed in [6] the use of reconstruction schemes of order high enough is fundamental for the accurate evolution of these systems and in particular for assessing the impact of the magnetic fields. Therefore all the results presented here have been computed using the PPM reconstruction, while the Harten-Lax-van Leer-Einfeldt (HLLE) approximate Riemann solver [24] has been used to compute the fluxes.

In order to guarantee the divergence-free character of the MHD equations we have employed the flux-CD approach described in [25], but with the difference that we adopt as evolution variable the vector potential instead of the magnetic field. In other words, by using an expression similar to equation (31) of [25], we compute the electric field at the center of each numerical cell by interpolating the fluxes computed at the interfaces of the cell and then use it to evolve directly the vector potential. We recall that in ideal MHD a relation exists between the fluxes of the magnetic field $\vec{B}$ and the value of the electric field $\vec{E} \equiv -\vec{\tilde{v}} \times \vec{\tilde{B}}$, where

$$\tilde{B}^i \equiv \sqrt{\gamma} B^i \,, \tag{1}$$
$$\tilde{v}^i \equiv \alpha v^i - \beta^i \,, \tag{2}$$

and where γ is the determinant of the 3-metric, v^i is the 3-velocity of the fluid as measured by an Eulerian observer, α the lapse, and β^i the shift vector. In particular, the following relations hold in Cartesian coordinates

$$E_x = \tilde{F}^z(\tilde{B}^y) = -\tilde{F}^y(\tilde{B}^z) \,, \tag{3}$$
$$E_y = -\tilde{F}^z(\tilde{B}^x) = \tilde{F}^x(\tilde{B}^z) \,, \tag{4}$$
$$E_z = \tilde{F}^y(\tilde{B}^x) = -\tilde{F}^x(\tilde{B}^y) \,, \tag{5}$$

with

$$\tilde{F}^i(\tilde{B}^j) \equiv \tilde{v}^i \tilde{B}^j - \tilde{v}^j \tilde{B}^i \,. \tag{6}$$

The evolution equations for the vector potential $\vec{A}$ and for the magnetic field $\vec{B}$ can then be written as

$$\partial_t \vec{A} = -\vec{E} \,, \tag{7}$$
$$\vec{\tilde{B}} = \vec{\nabla} \times \vec{A} \,. \tag{8}$$

Equation (7) is solved at the center of each cell (i, j, k), where the electric field is given by

$$E_x(x_i, y_j, z_k) = \frac{1}{4}\left(-\tilde{F}^y(\tilde{B}^z)_{(i,j+1/2,k)} - \tilde{F}^y(\tilde{B}^z)_{(i,j-1/2,k)} + \tilde{F}^z(\tilde{B}^y)_{(i,j,k+1/2)} + \tilde{F}^z(\tilde{B}^y)_{(i,j,k-1/2)}\right), \qquad (9)$$

$$E_y(x_i, y_j, z_k) = \frac{1}{4}\left(\tilde{F}^x(\tilde{B}^z)_{(i+1/2,j,k)} + \tilde{F}^x(\tilde{B}^z)_{(i-1/2,j,k)} - \tilde{F}^z(\tilde{B}^x)_{(i,j,k+1/2)} - \tilde{F}^z(\tilde{B}^x)_{(i,j,k-1/2)}\right), \qquad (10)$$

$$E_z(x_i, y_j, z_k) = \frac{1}{4}\left(-\tilde{F}^x(\tilde{B}^y)_{(i+1/2,j,k)} - \tilde{F}^x(\tilde{B}^y)_{(i-1/2,j,k)} + \tilde{F}^y(\tilde{B}^x)_{(i,j+1/2,k)} + \tilde{F}^y(\tilde{B}^x)_{(i,j-1/2,k)}\right), \qquad (11)$$

$\tilde{F}^i(\tilde{B}^j)$ being the numerical flux computed at the interface of the cell.

Since the magnetic field is computed from the curl of the vector potential using the same differential operator used to compute its divergence (*i.e.,* a central-difference scheme), its divergence free character is guaranteed at essentially machine precision at all times, also when using AMR. We note that a similar approach has been recently implemented also in another code [26] and, in analogy with [26], we add a Kreiss–Oliger type of dissipation [27] to the evolution equation of the vector potential in order to avoid the possible formation of spurious post-shock oscillations in the magnetic-field evolution. It has indeed been shown by [28] that applying TVD operators to the vector potential does not guarantee automatically the TVD character of the magnetic field, leading to possible post-shock oscillations in the latter. The code has been validated against a series of tests in special relativity [29] and in full general relativity (see [18]).

The system of GRMHD equations is closed by an EOS and, as discussed in detail in [2], the choice of the EOS plays a fundamental role in the post-merger dynamics and significantly influences the survival time against gravitational collapse of the HMNS produced by the merger.

As already done in [6], also in this paper we have employed the commonly used "ideal-fluid" EOS, in which the pressure p is expressed as $p = \rho\epsilon(\Gamma - 1)$, where ρ is the rest-mass density, ϵ is the specific internal energy and Γ is the adiabatic exponent. Such an EOS, while simple, provides a reasonable approximation and we expect that the use of realistic EOSs would not change the main results of this work.

B. Adaptive Mesh Refinements

Both the Einstein and the GRMHD equations are solved using the vertex-centered adaptive mesh-refinement (AMR) approach provided by the `Carpet` driver [30]. Our rather basic form of AMR consists in centering the highest-resolution level around the peak in the rest-mass density of each star and in moving the "boxes" following the position of this maximum as the stars orbit. The boxes are evolved as a single refinement level when they overlap.

The results presented below refer to simulations performed using 6 levels of mesh refinement with the finest level having a resolution of $h = 0.1500\,M_\odot \simeq 221\,\text{m}$. The grid structure is such that the size of the finest grids is $24\,M_\odot \simeq 35.4\,\text{km}$, while a single refinement level covers the region between a distance $r = 164\,M_\odot \simeq 242.2\,\text{km}$ and $r = 254.4\,M_\odot \simeq$

$375.7\,\text{km}$ from the center of the domain. This region is the one in which our gravitational-wave extraction is carried out, with a resolution of $h = 4.8\,M_\odot \simeq 7.1\,\text{km}$ (as a comparison, the gravitational wavelength is about $100\,\text{km}$ and thus well-resolved on this grid). In addition, a set of refined but fixed grids is set up at the center of the computational domain so as to better capture the details of the Kelvin-Helmholtz instability (*cf.* [2]). Moreover, after the merger, at about 8.5ms, we enlarge the central grid that is formed by the merging of the two initial boxes. We do this in order to cover a cubical region with a side of about $88.6\,\text{km}$ and so better resolve not only the whole HMNS, but also the BH-torus system which is produced by the collapse of the HMNS. For all the simulations reported here we have used a reflection-symmetry condition across the $z = 0$ plane and a π-symmetry condition across the $x = 0$ plane[2]. At the outer boundary we instead used simple zeroth-order extrapolation on the MHD variables (in practice, we just copy the value of the MHD quantities from the outermost evolved point in each direction to the points of the outer boundary in that direction). Also note that a very little amount of matter and magnetic fields reaches the outer boundary, so the effect of the outer-boundary conditions on the MHD and hydrodynamical variables is negligible.

The timestep on each grid is set by the Courant condition (expressed in terms of the speed of light) and so by the spatial grid resolution for that level; the Courant coefficient is set to be 0.35 on all refinement levels. The time evolution is carried out using 4th-order–accurate Runge-Kutta integration algorithm. Boundary data for finer grids are calculated with spatial prolongation operators employing 3rd-order polynomials for the matter variables and 5th-order polynomials for the spacetime variables. The prolongation in time employs 2nd-order polynomials and this ensures a significant memory saving, requiring only three timelevels to be stored, with little loss of accuracy due to the long dynamical timescale relative to the typical grid timestep.

The grid setup used here is therefore quite different from the one adopted in our previous work on magnetized NS binaries [6], where we had used fixed mesh-refinement in order to reduce the violation (generated by the interpolation in the buffer zones) of the divergence-free constraint of the magnetic field. Our current implementation, based of the evolution of the vector potential, does not produce any violation of the

---

[2] Stated differently, we evolve only the region $\{x \geq 0, z \geq 0\}$ applying a $180°$-rotational-symmetry boundary condition across the plane at $x = 0$.

TABLE I: Properties of the eight equal-mass binaries considered: proper separation between the stellar centers d/M_{ADM}; baryon mass M_b of each star; total ADM mass M_{ADM}; angular momentum J; initial orbital angular velocity Ω_0; mean coordinate radius r_e along the line connecting the two stars; ratio of the polar to the equatorial coordinate radii r_p/r_e; maximum rest-mass density $\rho_{\max}$; maximum initial magnetic field B_0, where $*$ is 8, 10 or 12. Note that M_{ADM} and J are reported as measured on the finite-difference grid.

Binary	d/M_{ADM}	$M_b\,(M_\odot)$	$M_{\mathrm{ADM}}\,(M_\odot)$	$J\,(\mathrm{g\,cm^2/s})$	$\Omega_0\,(\mathrm{rad/ms})$	r_e (km)	r_p/r_e	$\rho_{\max}\,(\mathrm{gm/cm^3})$	B_0 (G)
M1.45-B*	14.4	1.445	2.680	6.5084×10^{49}	1.78	15.0 ± 0.3	0.899	4.58×10^{14}	0 or $1.97 \times 10^*$
M1.62-B*	13.3	1.625	2.981	7.7806×10^{49}	1.85	13.6 ± 0.3	0.931	5.91×10^{14}	0 or $1.97 \times 10^*$

divergence-free condition of the magnetic field, since it interpolates the vector potential instead of the magnetic field in the buffer zones. Moreover, since the vector potential is stored at the center of the cell, it is possible to use without modification the prolongation and restriction operators currently available in the Carpet driver. This makes possible the use of the moving-grid setup that has been utilized with success in our previous general-relativistic hydrodynamics simulations.

C. Initial data

The initial data are the same used in [2, 6]. They were produced by Taniguchi and Gourgoulhon [31] with the multi-domain spectral-method code LORENE [32]. The initial solutions for the binaries are obtained assuming a quasi-circular orbit, an irrotational fluid-velocity field, and a conformally-flat spatial metric. The matter is modeled using a polytropic EOS $p = K\rho^\Gamma$ with $K = 123.6$ and $\Gamma = 2$, in which case the maximum gravitational mass is $M_{\mathrm{ADM}} \simeq 1.82\,M_\odot$ for a nonrotating star and $M_{\mathrm{ADM}} \simeq 2.09\,M_\odot$ for a uniformly rotating one. Since no self-consistent solution is available for magnetized binaries yet, a poloidal magnetic field is added a-posteriori using the vector potential

$$A_\phi \equiv \varpi^2 A_b \max\left(p - p_{\mathrm{cut}}, 0\right)^{n_s}, \qquad (12)$$

where $\varpi \equiv \sqrt{x^2 + y^2}$, $A_b > 0$ parameterizes the strength of the magnetic field, p_{cut} defines where in the NS the magnetic field goes to zero, and n_s determines the degree of differentiability of the potential. The components of the magnetic field are then computed by taking the curl of the Cartesian components of Eq. (12) to enforce that the divergence of the magnetic field is zero at machine precision. Here we have set $p_{\mathrm{cut}} = 0.04\max(P)$, and $n_s = 2$ to enforce that both the magnetic field and its first derivative are zero at $p = p_{\mathrm{cut}}$. In Ref. [3] the magnetic field was built with an expression equivalent to (12), but with p_{cut} set to the pressure in the atmosphere, and in Ref. [5] the expression used is slightly different and P_{cut} is set to be $4\% - 0.1\%$ of $\max(p)$; in both Refs. [3] and [5] $n_s = 1$.

Table I lists some of the properties of the eight equal-mass binaries considered here. More specifically, we have considered two classes of binaries differing in the initial masses, *i.e.*, binaries M1.45-B*, and binaries M1.62-B*. For each of these classes we have considered four different magnetizations (indicated by the asterisk) so that, for instance, M1.45-B12 is a low-mass binary with a maximum initial

magnetic field $B_0 = 1.97 \times 10^{12}$ G. Note that the binaries with zero magnetic fields are the same as those evolved in Ref. [2].

D. Gravitational-Wave Extraction

Details about the algorithms implemented in the code to extract the GW signal can be found in [2]. Here we just remind the reader that we compute the waveforms using two different methods. The first one is based on the Newman-Penrose formalism and computes the Weyl scalar Ψ_4. The gravitational-wave polarization amplitudes h_+ and $h_\times$ are then related to Ψ_4 by simple time integrals [33]

$$\ddot{h}_+ - \mathrm{i}\ddot{h}_\times = \Psi_4 , \qquad (13)$$

where the double overdot stands for the second-order time derivative.

The second method is instead based on the measurements of the nonspherical gauge-invariant perturbations of a Schwarzschild BH (see refs. [34–36] for some applications of this method to Cartesian-coordinate grids). In practice, a set of "observers" is placed on 2-spheres of fixed radius where we extract the gauge-invariant, odd-parity (or *axial*) current multipoles $Q^\times_{\ell m}$ and even-parity (or *polar*) mass multipoles $Q^+_{\ell m}$ of the metric perturbation [37, 38]. The $Q^+_{\ell m}$ and $Q^\times_{\ell m}$ variables are related to h_+ and $h_\times$ as [39]

$$h_+ - \mathrm{i}h_\times = \frac{1}{\sqrt{2}r} \sum_{\ell,m} \left(Q^+_{\ell m} - \mathrm{i}\int_{-\infty}^t Q^\times_{\ell m}(t')dt' \right) {}_{-2}Y^{\ell m} . \qquad (14)$$

Here ${}_{-2}Y^{\ell m}$ are the $s = -2$ spin-weighted spherical harmonics and (ℓ, m) are the indices of the angular decomposition.

Since the two methods have demonstrated to give waveforms that are identical up to the truncation error, we will here use h_+ computed only with the gauge-invariant quantities and we will focus only on the $\ell = 2, m = 2$ mode since the others have amplitudes which are negligible compared to this. All the waveforms have been extracted at a radius $r_{\mathrm{iso}} = 200M_\odot \approx 300\,\mathrm{km}$. We also ignored the contribution from the spherical harmonics since they depend on the direction of the source with respect to the detector and contribute as a multiplication factor of order 1 and so do not modify the results presented here.
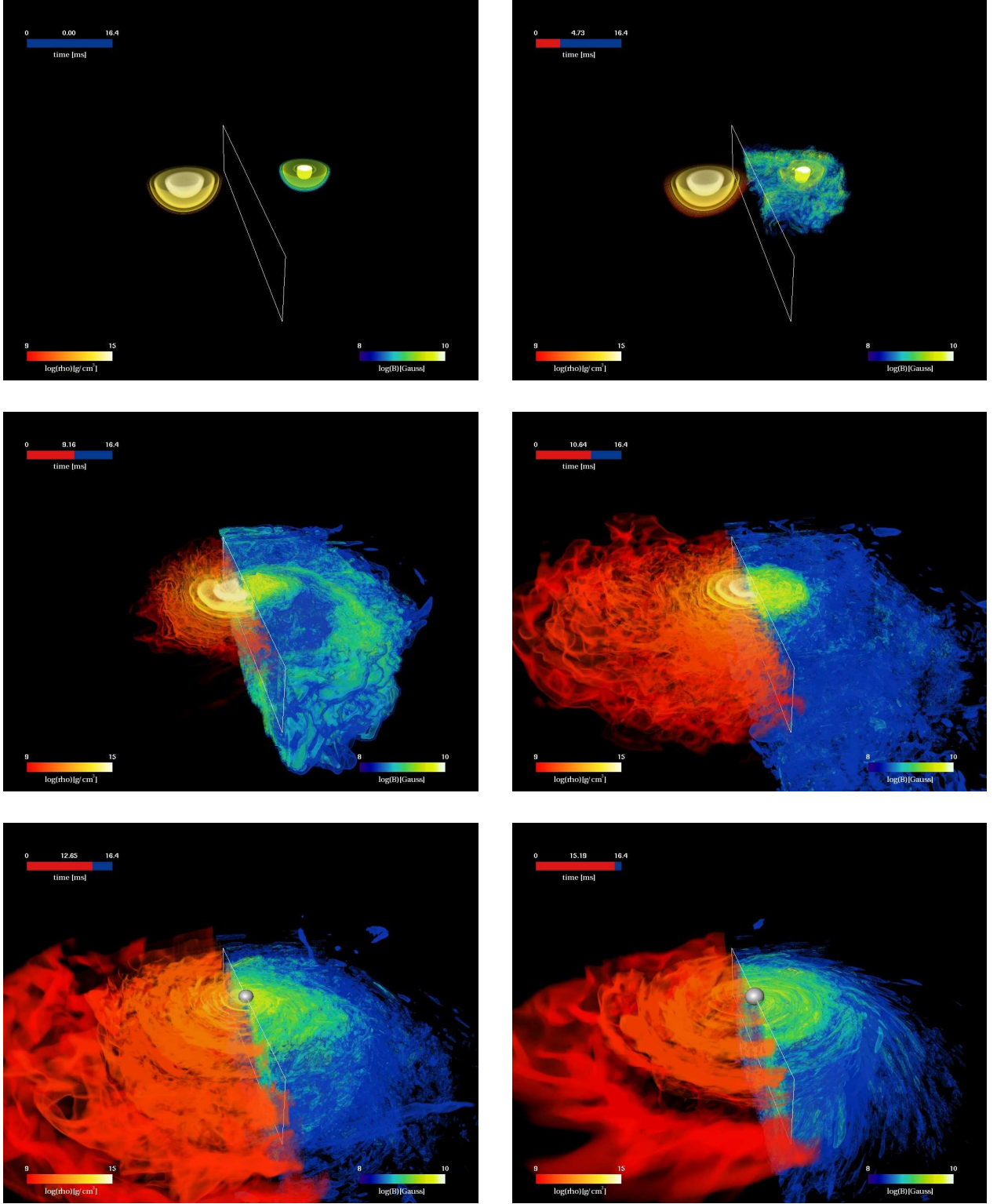
FIG. 1: Snapshots at representative times of the evolution of the high-mass binary with initial maximum magnetic field of 10^{10} G, *i.e.,* M1.62-B10. Shown with two different color-code maps are the rest-mass density ρ (red-yellow) and the magnetic field $|B|$ (blue-green-yellow-white). To better visualize the inner structure we plot only the values on $z < 0$. In order to show the two scalar quantities at the same time, they are shown on either side of a fictitious screen (ρ on the left and $|B|$ on the right). The first four panels refer respectively to the binary at the initial separation of 45 km, to the binary after two orbits, to the merger and to the bar-deformed HMNS. The last two panels, instead, refer respectively to when the BH has just been formed and to a subsequent stage of the quasi-stationary evolution of the BH-torus system. The grey spheroidal surface in the center represents the location of the apparent horizon.

E. Accuracy of the Results

A reliable assessment of the truncation error is essential to draw robust conclusions on the results of numerical simulations. Following a procedure discussed in detail in Ref. [4], also here we have carried out a systematic measurement of the accuracy and convergence properties of our simulations, and deduced a corresponding *"error-budget"*. The main conclusions are very similar to those drawn in Ref. [4], which for compactness only we briefly recall here. More specifically, we showed that with typical (finest) resolutions of $h \sim 0.12 \, M_\odot - 0.19 \, M_\odot$, the results show the expected convergence rate of 1.8 during the inspiral phase, which however drops to 1.2 at the merger and during the evolution of the HMNS. This deterioration of the convergence rate is due mostly to the strong shocks which form during the merger and which HRSC schemes can reproduce at 1st-order only. Furthermore, physical quantities, such as the rest-mass, are conserved with a relative error of $\lesssim 10^{-6}$, while the energy and the angular momentum is conserved to $\lesssim 1\%$ after taking into account the parts lost to radiation. Finally, the expected agreement in both phase and amplitude is found in the waveforms extracted from different detectors within the same simulation or from the same detector but at different resolutions. Such waveforms have been found to be also convergent at a rate of 1.8 (see [4] for details). Finally, for all the simulations reported here the violation of the Hamiltonian constraint has an L2-norm which is $\lesssim 10^{-4}/M_{\rm ADM}^2$ for the high-mass binaries and $\lesssim 10^{-5}/M_{\rm ADM}^2$ for the low-mass ones, for which no BH is formed.

III. BINARY DYNAMICS

As mentioned above, in order to highlight some of the most salient aspects of the binary dynamics it will be sufficient to consider two main classes of initial configurations: M1.62-B* and 1.45-B*. These models differ only in the mass, the first being composed of stars each having a rest mass of $1.625 \, M_\odot$ (which we refer to as the *"high-mass binaries"*), the second of stars of rest mass $1.445 \, M_\odot$ (which we refer to as the *"low-mass binaries"*). The use of these two classes is useful to distinguish the phenomenology of binaries whose merger leads to a prompt collapse of the HMNS from those where the HMNS can instead survive for several tens of milliseconds and up to a fraction of a second (see the discussion in [2]). We also note that in the case of the unmagnetized models, the dynamics are the same as the one described in [2], to which we refer the interested reader for a more detailed description of the evolution of the matter and of the hydrodynamical instabilities such as the Kelvin-Helmholtz instability.

A synthetic overview of the dynamics is summarized in Fig. 1, which shows snapshots at representative times of the evolution of the high-mass binary with initial maximum magnetic field of $10^{10} \, \mathrm{G}$, *i.e.,* M1.62-B10. Shown with two different color-code maps are the rest-mass density ρ (red-yellow) and the magnetic field $|B|$ (blue-green-white). To better visualize the inner structure we plot only the values

on $z < 0$. In order to show the two scalar quantities at the same time, they are shown on either side of a fictitious screen (ρ on the left and $|B|$ on the right). The first four panels refer respectively to the binary at the initial separation of 45 km ($t = 0 \, \mathrm{ms}$), to the binary after two orbits ($t = 4.7 \, \mathrm{ms}$), to the merger ($t = 9.2 \, \mathrm{ms}$) and to the bar-deformed HMNS ($t = 10.6 \, \mathrm{ms}$). The last two panels, instead, refer respectively to when the BH has just been formed ($t = 12.6 \, \mathrm{ms}$) and to a subsequent stage of the quasi-stationary evolution of the BH-torus system ($t = 15.2 \, \mathrm{ms}$).

With this overall qualitative behaviour of the binary in mind, we will next consider a more quantitative discussion of the evolution of the magnetic fields and we will only briefly summarize the dynamics of the matter. In doing this we will present in Figs. 2 and 3 the evolution of both the high and low-mass binaries to aid the comparison between the two classes of models.

A. High-mass binaries

We start by considering the evolution of the high-mass binaries M1.62-B*, some of which systems were already considered in [6], where it was shown that initial magnetic fields lower than 10^{14} G do not affect the dynamics in the inspiral phase. Overall, given the initial coordinate separation of $45 \, \mathrm{km}$, all binaries inspiral for approximately 3 orbits before merging at $t \approx 8.2 \, \mathrm{ms}$. There are different ways to measure the time of the merger and the one we adopt here consists in looking at the first peak in the evolution of $|\Psi_4|$. This time corresponds approximately to when the two stellar cores merge and we note that the external layers of the stars enter into contact about $2 \, \mathrm{ms}$ earlier. In the top panel of the left column of Fig. 2 we show the evolution of the maximum of the rest-mass density $\rho_{\rm max}$ normalized to its initial value. It is particularly clear from the evolution of $\rho_{\rm max}$ that all the models merge at the same time (e.g. see the first minimum in the evolution), while the post-merger dynamics are quite different. All the models form an HMNS that survives a few milliseconds before collapsing to a Kerr BH, but its survival time varies considerably, as well as the number of oscillations in the evolution of the density before the rapid exponential increase in correspondence with the collapse. A discussion about this will be presented in the following Section III B.

The middle panel of the left column of Fig. 2 shows instead the maximum of the absolute value of the divergence of the magnetic field. To the best of our knowledge this is the first time that the evolution of the divergence of the magnetic field is shown in a GRMHD simulation of BNSs. Because this is a fundamental quantity to evaluate the quality of a numerical calculation, we encourage other authors to present it systematically as well. As expected on mathematical grounds, the implementation of the GRMHD equations discussed in Sect. II A is such that the divergence of the magnetic field is essentially at machine precision at all times. It is important to stress that such a small violation would not be possible with the cell-centred AMR algorithm provided by the Carpet code unless the vector potential is used as an evolved variable.
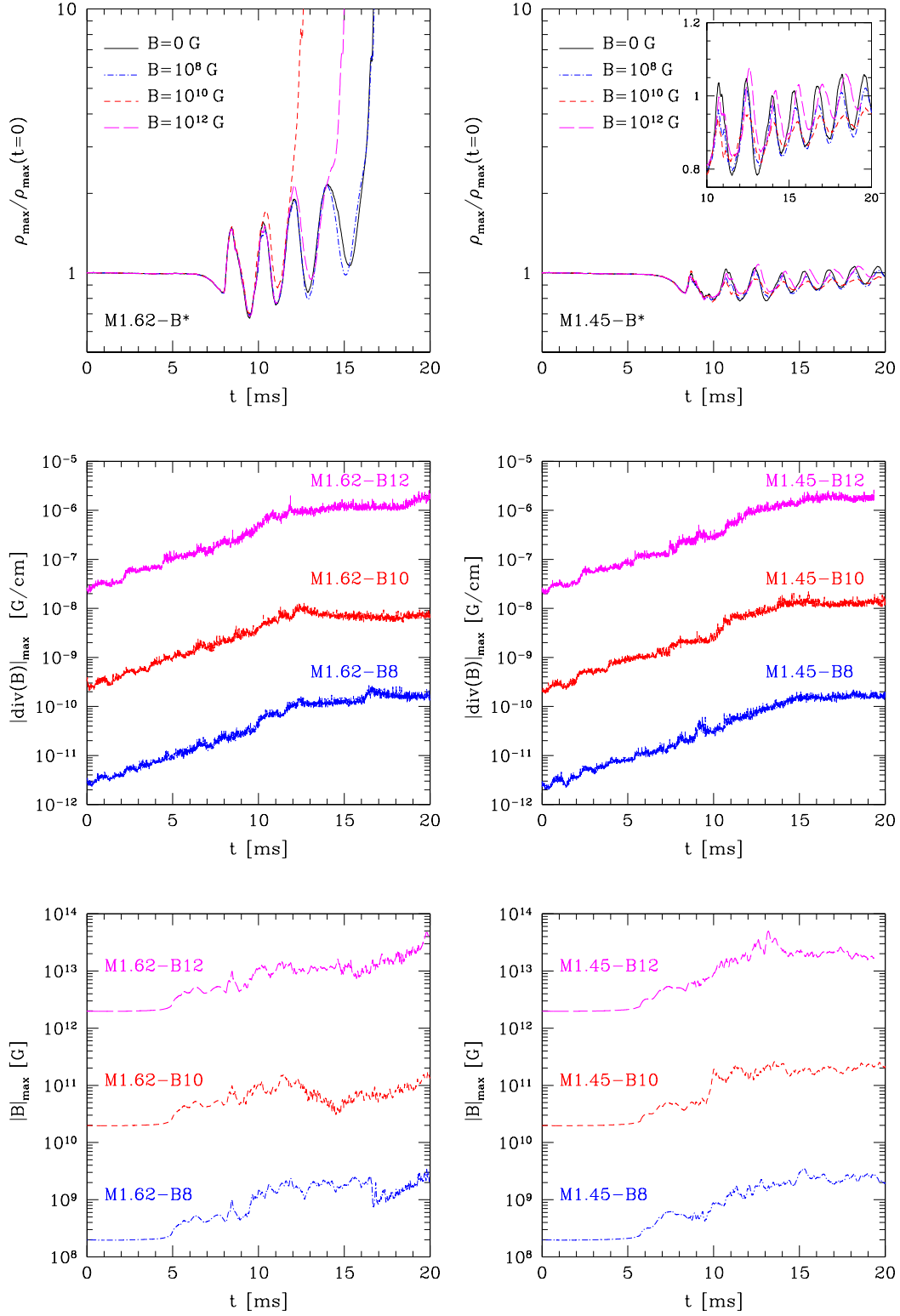
FIG. 2: Evolution of the maximum of the rest-mass density ρ normalized to its initial value (top row), of the maximum of the absolute value of the divergence of B (middle row), and of the maximum of the magnetic field strength $|B|$ (bottom row). The left and right columns refer to the high-mass and low-mass binaries, respectively. Note that in the case of the high-mass models (left column), the values of $|B_{\max}|$ after BH formation refer, for the large majority of the time, to matter outside the apparent horizon and in the torus.
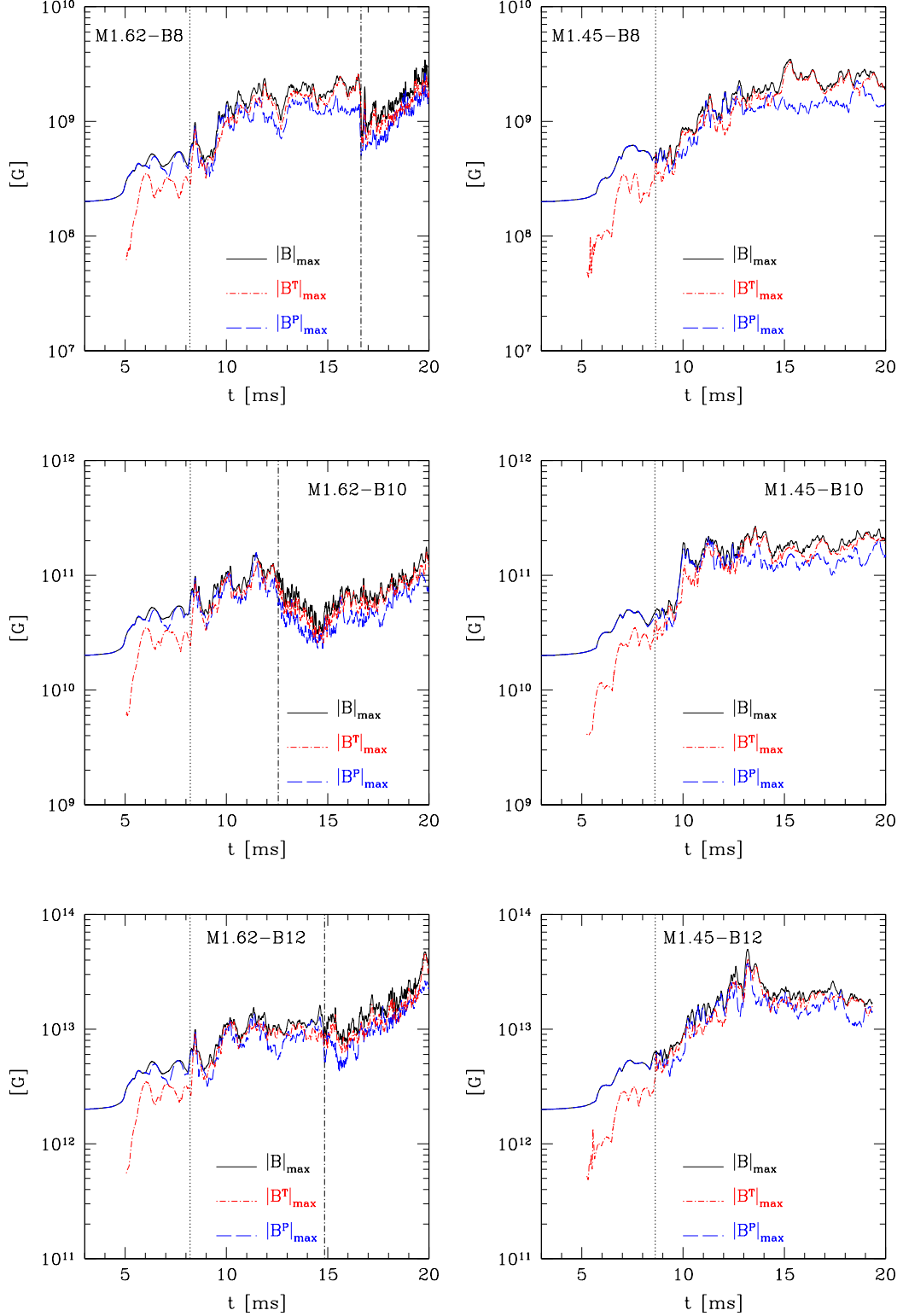
FIG. 3: Evolution of the maximum magnetic field strength $|B|_{max}$ (black solid line) and of its poloidal $|B^P|_{max}$ (blue long-dashed line) and toroidal $|B^T|$ (red short-dashed line) components during and after the merger. The left column refer to the high-mass model while the right one to the low-mass case. The vertical dashed lines refer to the time of the merger and of the collapse (measured respectively as the first and last peaks in the evolution of $|\Psi_4|$). Since the simulations of the low-mass binaries were not carried on until the collapse, only the time of the merger is shown in the panels in the right column.
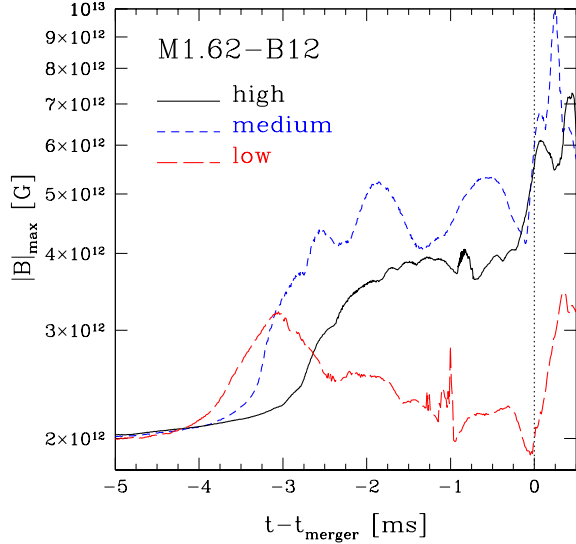
FIG. 4: Evolution of the maximum magnetic field strength $|B|_{\max}$ for the high-mass model M1.62-B12 evolved with three different resolutions: $h = 177\,\mathrm{m}$ (high resolution, black solid line), $h = 221\,\mathrm{m}$ (medium resolution, blue short-dashed line) and $h = 354\,\mathrm{m}$ (low resolution, red long-dashed line). The curves have been shifted in time to account for the slightly different time of the merger.

Finally, the bottom panel of the left column of Fig. 2 shows that the magnetic field grows mostly at the time of the merger and reaches values which are about one order of magnitude higher, before the collapse to BH. We note that in the case of the high-mass models (left column) the values of $|B_{\max}|$ after BH formation refer, for the large majority of the time, to matter outside the apparent horizon and in the torus. This is because the steep gradients of the matter variables inside the apparent horizon are under-resolved as a result of the grid stretching and dissipated on a timescale which is of the order of a fraction of a ms. Hence, with a few possible exceptions, the data in the plots refers statistically to the matter outside the apparent horizon.

The growth of the magnetic field at the merger is made more clear in the different panels contained in the left column of Fig. 3, where we concentrate in particular on the evolution of the maxima of the total magnetic field (black solid line) and of its toroidal (red dot-dashed line) and poloidal (blue long-dashed line) components. As already shown in [2], Kelvin-Helmholtz instability develops during the merger, when the external layers of the two NSs enter into contact, *i.e.,* roughly $2\,\mathrm{ms}$ before the time of the merger, which is indicated in those panels with the first vertical dotted line. This purely hydro-dynamical instability leads to the formation of vortices that can curl magnetic field lines that were initially purely poloidal and produce toroidal components. As it is evident from the panels in Fig. 3, a strong toroidal component is indeed formed in all cases and it reaches values that are comparable or larger than the poloidal component, but its energy is not in equipartition with the kinetic energy in the layer. Despite the exponential

growth caused by the Kelvin-Helmholtz instability, the overall amplification of the magnetic field is of an order of magnitude at most, with a growth rate $dB/dt \sim 2 \times 10^{12}\,(\mathrm{G/ms})$ in the case of model M1.62-B12. This is in contrast with what reported by [40], where an amplification of several orders of magnitude in the magnetic field of the HMNS was observed, with a growth rate $dB/dt \sim 2 \times 10^{15}\,(\mathrm{G/ms})$ for a model similar to M1.62-B12.

It is presently unclear what is the origin of this discrepancy. It is possible that this is due to the use of very different numerical techniques, namely smooth-particle hydrodynamics and HRSC methods. It is also possible that although we have used the largest resolutions employed so far in simulations of magnetized BNSs, such resolutions are not yet sufficient to properly resolve the nonlinear development of the instability. Studies of the effect of these instabilities and of the consequent amplification of the magnetic fields have recently been performed with local simulations on simpler backgrounds [41, 42]. These studies have indeed shown that in order to achieve convergence in the vortex region it is necessary to use resolutions that are much higher than those currently affordable in BNS simulations. On the other hand, by performing simulations with different resolutions for model M1.62-B12 we did not observe any sensible difference in the amplification of the magnetic field and indeed the magnetic field evolution is certainly consistent if not convergent (see the discussion in [4] about why it is difficult to determine the convergence order after the merger). This is shown in Fig. 4, where we report the evolution of the maximum magnetic field strength $|B|_{\max}$ for the high-mass model M1.62-B12 evolved with three different resolutions: $h = 177\,\mathrm{m}$ (high resolution, black solid line), $h = 221\,\mathrm{m}$ (medium resolution, that is the standard resolution used in this article, blue short-dashed line) and $h = 354\,\mathrm{m}$ (low resolution, red long-dashed line). The curves have been shifted in time to account for the slightly different time of the merger. It is clear that that doubling the resolution produces a difference in the amplification of less than a factor ~ 2 (compare the red long-dashed line with the black solid line); the differences become even smaller when comparing the medium and high resolution[3]. A similar consistency with resolution is not present in the simulations reported in [40], where the differences among the amplified magnetic fields seem even to become larger with increasing resolution[4].

Overall we believe that the main reason why the toroidal magnetic field in our simulations does not grow significantly at the merger is that the timescale over which the instability can develop is rather short. The shear layer between the two stars, in fact, survives only for about $1\,\mathrm{ms}$, before being

---

[3] Figure 4 also shows a considerable increase in the magnetic field at the merger. However, this is not related to the Kelvin-Helmholtz instability, but rather to flux conservation which amplifies the magnetic field when the matter is compressed by the collision of the two stellar cores.

[4] Note that because we are here capturing a non-sustained turbulent flow, the variations of the magnetic field strength with resolution are not necessarily monotonic.

destroyed by the collision between the two stellar cores. In Refs. [41, 42], the amplification of the magnetic field has been observed on timescales that are even shorter than this one, but only under very specific conditions and only for specific values of the velocity at the shear layer. The differences between the condition under which the instability develops in our fully general-relativistic simulations and those used in these local simulations may explain the different results. Clearly, the best way to assess whether or not the development of the Kelvin-Helmholtz instability leads to a large or only to a moderate field amplification is to perform direct comparisons with other general-relativistic simulations of magnetized BNSs. Unfortunately, so far the only other reported evolution of the magnetic field is the one in [6], which is clearly not useful for an independent comparison.

As a final remark, it is important to emphasize that the toroidal and poloidal components have comparable values also in the torus that is formed after the collapse to BH (*cf.* panels in the left column of Fig. 3). Since most of the simulations to date of magnetized accretion disks around BHs that model the central engine of short GRBs use initial conditions in which the magnetic field has only a poloidal component, it is of particular importance to remark that more realistic initial data should instead have a toroidal and a poloidal component of the comparable magnitude.

B. Delay of the Collapse

It has been shown and discussed in a number of works that when the merger leads to a collapse, the time of survival of the HMNS depends on several factors, which include: the EOS, the efficiency in the redistribution of angular momentum, and the efficiency of the radiative transfer. Clearly, all of these influencing factors will act differently in highly-magnetized matter and hence the delay time $\tau_{\rm d}$, *i.e.,* the time between the formation of the HMNS and its collapse to a BH, can be used to measure indirectly the magnetic fields of the progenitor NSs. There are several different ways of defining $\tau_{\rm d}$, but a convenient and gauge-invariant one is to consider the delay time as the interval between the first and last peak in the evolution of $|\Psi_4|$, which are always well-defined in the amplitude evolution, as these can be taken to correspond to the merger of the stellar cores and to the BH production.

In Fig. 5 we show therefore the survival time of the HMNS as a function of the initial magnetic field strength, together with the error bar as estimated from a set of simulations of unmagnetized binary NS mergers at different resolutions (the delay time converges at first order, increasing with resolution). It is clear from Fig. 5 that while models M1.62-B0 and M1.62-B8 have roughly the same post-merger dynamics and the same collapse time (see also the top left panel of Fig. 2), it is also clear that models M1.62-B10 and M1.62-B12 collapse earlier than the unmagnetized one. To understand why this is the case, we recall that magnetic fields can affect the dynamics of the HMNS as first shown in axisymmetric evolutions of an isolated differentially rotating HMNS [43, 44].
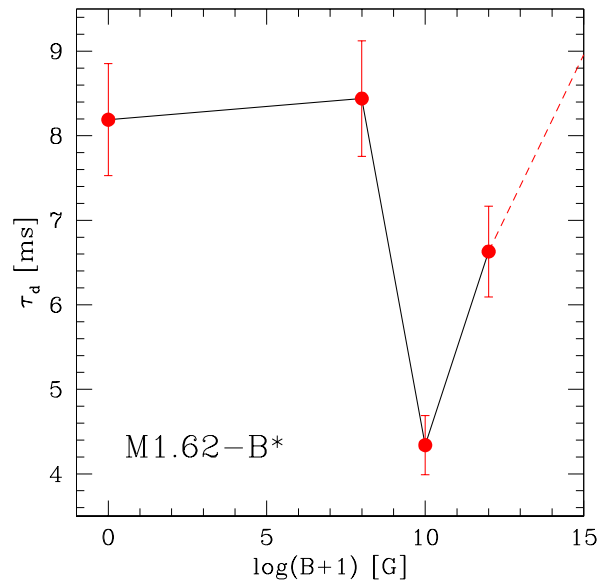

FIG. 5: Lifetime of the HMNS formed after the merger in the high-mass case as a function of the initial magnetic field. The error bar has been estimated from a set of simulations of unmagnetized binary NS mergers at three different resolutions; in particular, we have assumed that the magnetized runs have the same relative error on the delay time of the corresponding unmagnetized model. Indicated with a dashed line is the continuation of the delay times to ultra-high magnetic fields of 10^{17} G.

In essence, magnetic fields can, via magnetic tension[5], redistribute the angular momentum, transporting it outwards and reducing the amount of differential rotation that is essential in supporting the HMNS against gravitational collapse (we recall that a HMNS has, by definition, a mass which cannot be sustained by the star if rotating uniformly). The ratio between the magnetic tension and the pressure gradients scales like the ratio between the magnetic pressure and the gas pressure, and this ratio increases (although remaining less than one) after the merger because the magnetic fields are stronger and the HMNS is more extended and with smaller pressure gradients. As a result, magnetic fields can "accelerate" the collapse of these models, but only if sufficiently strong so that the magnetic tension can be comparable or larger than the normal pressure gradients. Hence, the efficiency in angular-momentum redistribution will be proportional to the intensity of the (square of the) magnetic field and this explains why the delay time is essentially unchanged for small magnetic fields, such as $B_0 \lesssim 10^8$ G. For larger values, how-

---

[5] We recall that in Newtonian ideal MHD the Lorentz force appearing in the equation for the conservation of momentum is given by

$$\frac{1}{4\pi\rho}\left[(\nabla \times \vec{B}) \times \vec{B}\right] = \frac{1}{4\pi\rho}\left[(\vec{B} \cdot \nabla)\vec{B} - \nabla\left(\frac{B^2}{2}\right)\right], \quad (15)$$

where in the right-hand side the first term is the "magnetic tension" along the field lines and the second one is the (isotropic) "magnetic pressure".
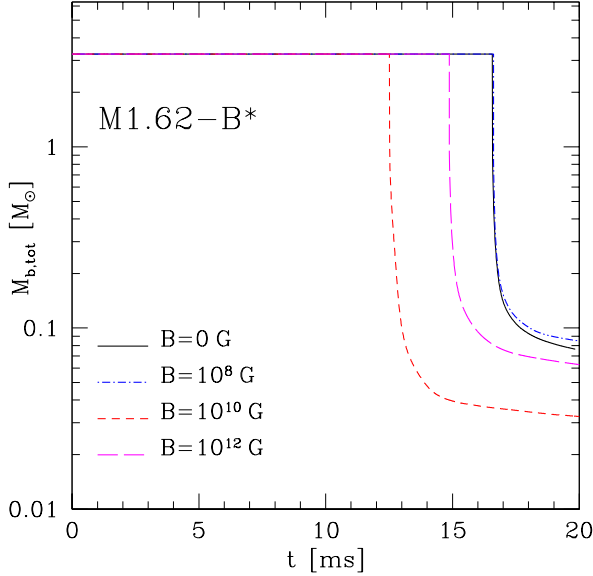
FIG. 6: Evolution of the total rest-mass for the different high-mass binaries considered. Note that the sudden drop corresponds to when the apparent horizon is formed since we exclude the region inside it from the computation of the mass. Note also that the early collapse of M1.62-B10 leads to tori which are about a factor of two less massive.

FIG. 7: Comparison of the properties of the tori produced either by a magnetized binary (M1.62-B12, blue dashed line) or by a un-magnetized one (M1.62-B0, red solid line). *Top panel:* rest-mass density along the x-axis at $\sim 3\,\text{ms}$ after the formation of the apparent horizon and which we truncate at $10^{10}\,\text{g/cm}^3$. *Bottom panel:* Angular velocity at the same time as above; shown as reference with a dotted line is the Keplerian angular velocity Ω_{Kep}, which matches very well the outer parts of the torus.

ever, the magnetic fields can influence the dynamics of the HMNS and decrease τ_{d} as shown by models M1.62-B10 and M1.62-B12.

Interestingly, the HMNS relative to the binary M1.62-B12 survives longer than the M1.62-B10 one. This should not be entirely surprising since a very large magnetic field will also introduce a magnetic pressure [*cf.* eq. (15)], which will provide an additional pressure support and thus either compensate or even dominate the angular-momentum redistribution. Indeed, when simulating a binary with an initial magnetic field of $B_0 \sim 10^{17}$ G we have found that the delay time increases and is even larger than the one obtained in the absence of a magnetic field. This is not shown directly in Fig. 5, which has been restricted to realistic values of the magnetic field, but we have indicated with a dashed line the continuation of the delay times to ultra-high magnetic fields. Clearly, because of this tight correlation between the degree of magnetization of the NS matter and the delay of the time of the collapse, the measurement of the latter via a GW detection will allow to infer the former.

The difference in the time of the collapse produces also small differences in the mass of the final BH and torus. This is shown in Fig. 6, which reports the evolution of the total rest-mass for the different high-mass binaries considered, and where the sudden drop corresponds to the formation of the apparent horizon (the matter inside the horizon is excluded from the computation of the baryon mass; see [45] for a discussion of the properties of the collapse with the gauge conditions used here). Similarly, in Table II we list the mass and spin of the BH formed at the end of the evolution, and the
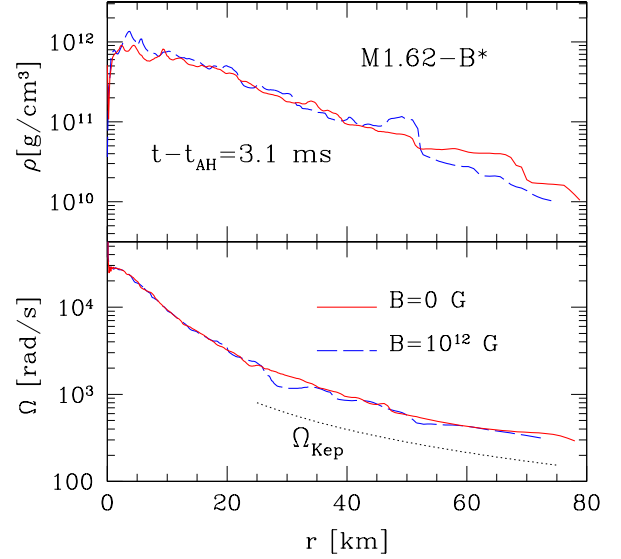
mass and radius of the torus. Since the models collapse at different times we have taken our measure at the end of the simulation (*i.e.*, at $t \simeq 20\,\text{ms}$), when the accretion onto the BH is small and essentially stationary. In all cases the mass of the BH is $M_{\text{BH}} \approx 2.9 M_{\odot}$ and the spin is $a \equiv J/M^2 \approx 0.8$, but the mass of the torus drops from about $0.063 - 0.085\,M_{\odot}$ to $0.033 M_{\odot}$ in the case of model M1.62-B10. This is probably due to the fact that the magnetic field causes some matter to move outside the core region and that will become a BH; as a result, the longer the delay time, the larger the tori. We note that, even if small, these tori could still provide sufficient energy to power short GRBs.

As a final remark we note that at least over the timescales considered here, the differences in the local dynamics of the torus matter between magnetized and unmagnetized binaries is very small. This is because the magnetic field is not yet strong enough to produce significant changes in the dynamics. A convincing example is shown in Fig. 7, which offers a comparison of the properties of the tori produced either by a magnetized binary (M1.62-B12, blue dashed line) or by a unmagnetized one (M1.62-B0, red solid line). The top panel, in particular, shows the rest-mass density along the x-axis at about $3\,\text{ms}$ after the formation of the apparent horizon and which we truncate at $10^{10}\,\text{g/cm}^3$. Besides small differences (the data refers to very different simulations), the density profiles are very similar. An analogous conclusion can be drawn when looking at the bottom panel, which shows the angular velocity at the same time as above; also reported as

TABLE II: Columns $2 - 3$ report the mass M and spin a of the BH, while column 4 shows the mass of the torus formed after the merger of the high-mass models, and column 5 the radius of the torus (computed as a mean of the position where the rest-mass density goes below $10^{10} \, \mathrm{gcm}^{-3}$ in the time interval between 19 and 20 ms). All the other quantities have been measured at $t = 20 \, \mathrm{ms}$), when the accretion onto the BH is small and essentially stationary.

Binary	$M \, [M_\odot]$	$a \equiv J/M^2$	$M_{\mathrm{tor}} \, [M_\odot]$	$r_{\mathrm{tor}} \, [\mathrm{km}]$
M1.62-B0	2.90	0.80	0.076	105 ± 13
M1.62-B8	2.89	0.80	0.085	102 ± 16
M1.62-B10	2.94	0.82	0.033	69 ± 4
M1.62-B12	2.91	0.81	0.063	94 ± 4

reference with a dotted line is the Keplerian angular velocity Ω_{Kep}, which matches very well the outer parts of the torus.

C. Low-mass binaries

As already shown in [6] and anticipated in the previous Section, also in the low-mass case the presence of an initial magnetic field introduces no significant modification in the evolution of the binaries during the inspiral. To compare directly with the behavior of the high-mass binaries, we show in the right column of Fig. 2 the evolution of the maximum of the rest-mass density normalized to its initial value, the maximum of the absolute value of the divergence of the magnetic field and the maximum of the magnetic field. We recall that in Ref. [8] it was shown that the low-mass models take more than $100 \, \mathrm{ms}$ to collapse to BH in the unmagnetized case, so the 20 ms of evolution of the present work are not sufficient to reach the collapse.

In the top panel it is possible to appreciate that the evolution of ρ_{max} for the unmagnetized case and those of the magnetized binaries are very similar, with only small differences in the frequency of the oscillations of the HMNS formed after the merger. Overall, the presence of a magnetic field decreases the oscillation frequency (*cf.* inset), probably because the additional magnetic tension counters the expansions of the bar-deformed HMNS. Moving over to the right bottom panel of Fig. 2, it is possible to note that also in the low-mass case all the magnetized models show an amplification of the magnetic field of about one order of magnitude and also in this case the divergence of the magnetic field is zero essentially at machine precision. As for the high-mass binaries, interesting point to note is that, on the timescale studied here, the magnetic field grows of about one order of magnitude soon after the merger (at $t \approx 8 \, \mathrm{ms}$), but then it saturates to a constant value.

Additional information about the magnetic-field evolutions for the three different models are given in the panels in the right column of Fig. 3. Also in this case the toroidal component of the magnetic field (red dot-dashed line) is amplified exponentially because of the Kelvin-Helmholtz instability at the time of the merger of the external layers of the stars and it reaches the same value of the poloidal component. Both components have comparable values for the remaining dura-

tion of the simulation and we expect that also in this case the collapse of the HMNS will produce a torus with a magnetic field configuration in which the toroidal and poloidal components have the same strength. This seems to be, at least for the equal-mass BNSs considered here, a universal characteristic of the tori that are formed from these systems.

IV. GRAVITATIONAL-WAVE EMISSION

A. High-mass binaries

In Fig. 8 we show the GW signals emitted by the 4 high-mass binaries considered in this paper. The top left panel shows the unmagnetized case, the top right panel the model with an initial magnetic field of 10^8 G, the bottom left panel $B \approx 10^{10}$ G and the bottom right panel $B \approx 10^{12}$ G. In the bottom right panel, together with M1.62-B12 (black solid line, which collapses at $t \approx 16 \, \mathrm{ms}$), we also show - to make the comparison clearer - the evolution of M1.62-B0 (red dashed line, which collapses later). All the waveforms exhibit very similar features and, with the exception for the different duration of the post-merger phase already discussed in Section III A, they are almost indistinguishable from each other. Therefore, for all the models the signal is essentially composed of three parts: the inspiral (from $t - r = 0 \, \mathrm{ms}$ to $t - r \approx 8 \, \mathrm{ms}$), the HMNS evolution (from $t - r \approx 8 \, \mathrm{ms}$ to $t - r \approx 13 - 17 \, \mathrm{ms}$) and the ring-down of the final BH. The high-frequency oscillations in the post-merger phase are due to the cores of the two NSs that repeatedly bounce against each other until a sufficient amount of angular momentum is extracted via GWs emission or is moved to the external layers of the HMNS via the magnetic-field tension. When this happens, the centrifugal support becomes insufficient to balance the gravitational forces and the HMNS is induced to collapse to a rotating BH with dimensionless spin $J/M^2 \simeq 0.80$ (*cf.* Table II). Such oscillations are directly related to the oscillations visible in the evolution of the maximum of the rest-mass density in the top-left panel of Fig. 2.

B. Low-mass binaries

In analogy with what done for the high-mass binaries, we show in Fig. 9 the GW signal for the low-mass models and also in this case the bottom right panel shows both the M1.45-B12 (black solid line terminated at $t - r \approx 19 \, \mathrm{ms}$) and M1.45-B0 (red dashed line) models for comparison. Since we have not evolved these models until the collapse of the HMNS to BH, only the inspiral and the post-merger phase (the part of the signal for $t - r \gtrsim 8.5 \, \mathrm{ms}$) are present in the GW signal. The high-frequency oscillations in the post-merger phase are related to the formation of a bar-deformed HMNS (as already described in [2]), whose spinning frequency is not significantly affected by the presence of magnetic fields. Also in this case, all the waveforms are very similar to each other both during the inspiral and after the merger. As a result, and in contrast with what seen for the high-mass
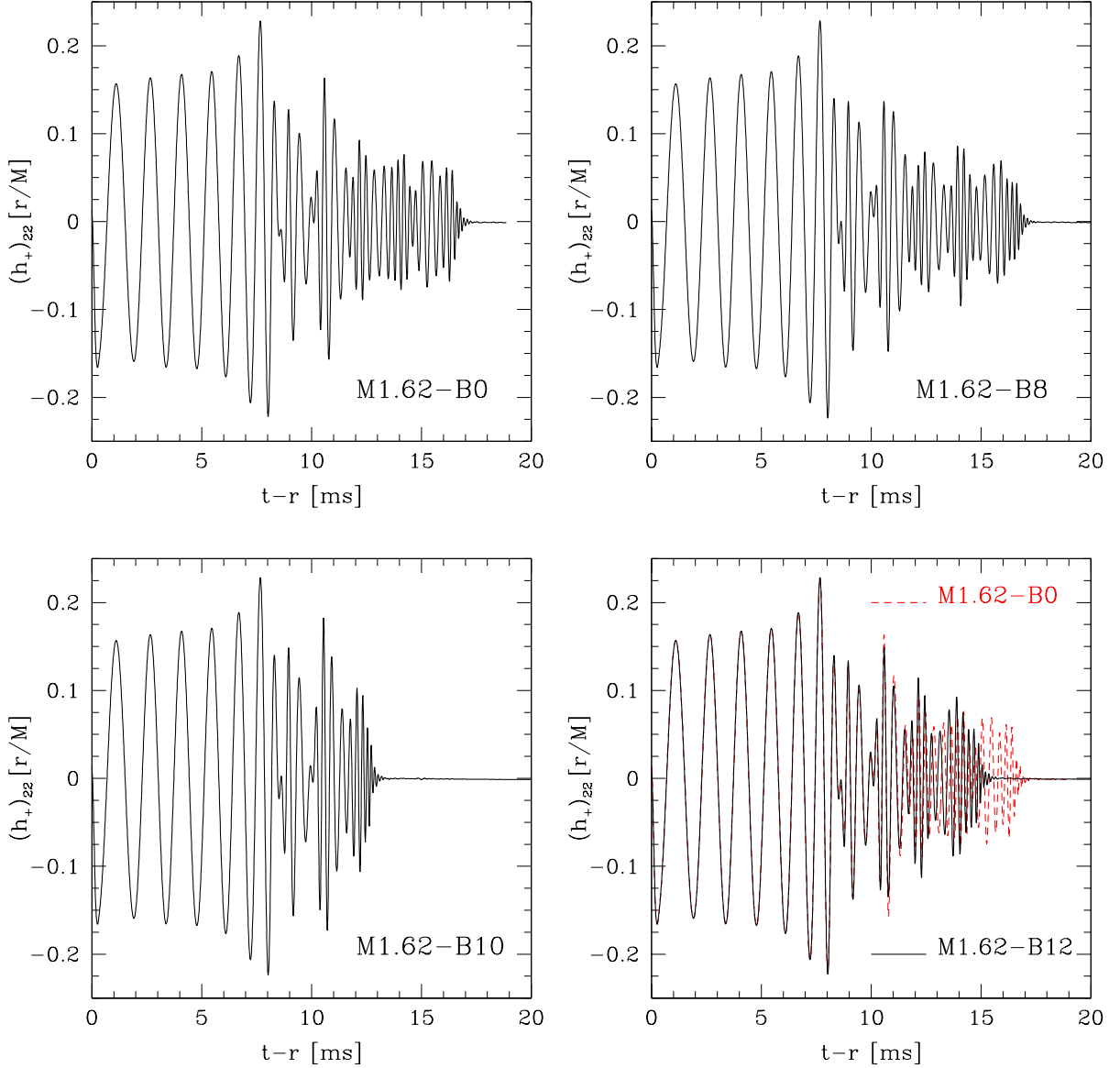
FIG. 8: Gravitational waves for the high-mass binaries as a function of the retarded time $t - r$ in ms. The last panel shows for comparison also the unmagnetized model (*i.e.,* red dashed line which collapses at $t - r \approx 17\,\text{ms}$) together with the model M1.62-B12 (black solid line which collapses earlier).

case, the differences in the phase evolution are very small, at least over the timescales considered here (*cf.* bottom right panel). Clearly, if the HMNS continues to exist for longer times (on the radiation-reaction timescale), then the small differences may grow sufficiently and lead to a detectable difference. While the numerical simulation of the secular evolution of the HMNS represents a challenge that we will address in future work, its impact on the detectability of the magnetic field will be further discussed in the next Section.

C. Detectability of the magnetic field

In order to assess the possibility of distinguishing between the different waveforms and hence establish whether different magnetizations of the HMNS can be measured, we have computed the power spectral densities of the GWs discussed before and plotted them in Fig. 10 against the sensitivity curves of different ground-based GW detectors. In particular, we show the scaled power spectral densities $\tilde{h}_+(f)f^{1/2}$ for the high-mass case (left panel) and low-mass case (right panel) with an initial magnetic field (dot-dashed red line) of $B \approx 10^8\,\text{G}$ (first row), $B \approx 10^{10}\,\text{G}$ (second row), and $B \approx 10^{12}\,\text{G}$ (third row). In all the panels the sources are
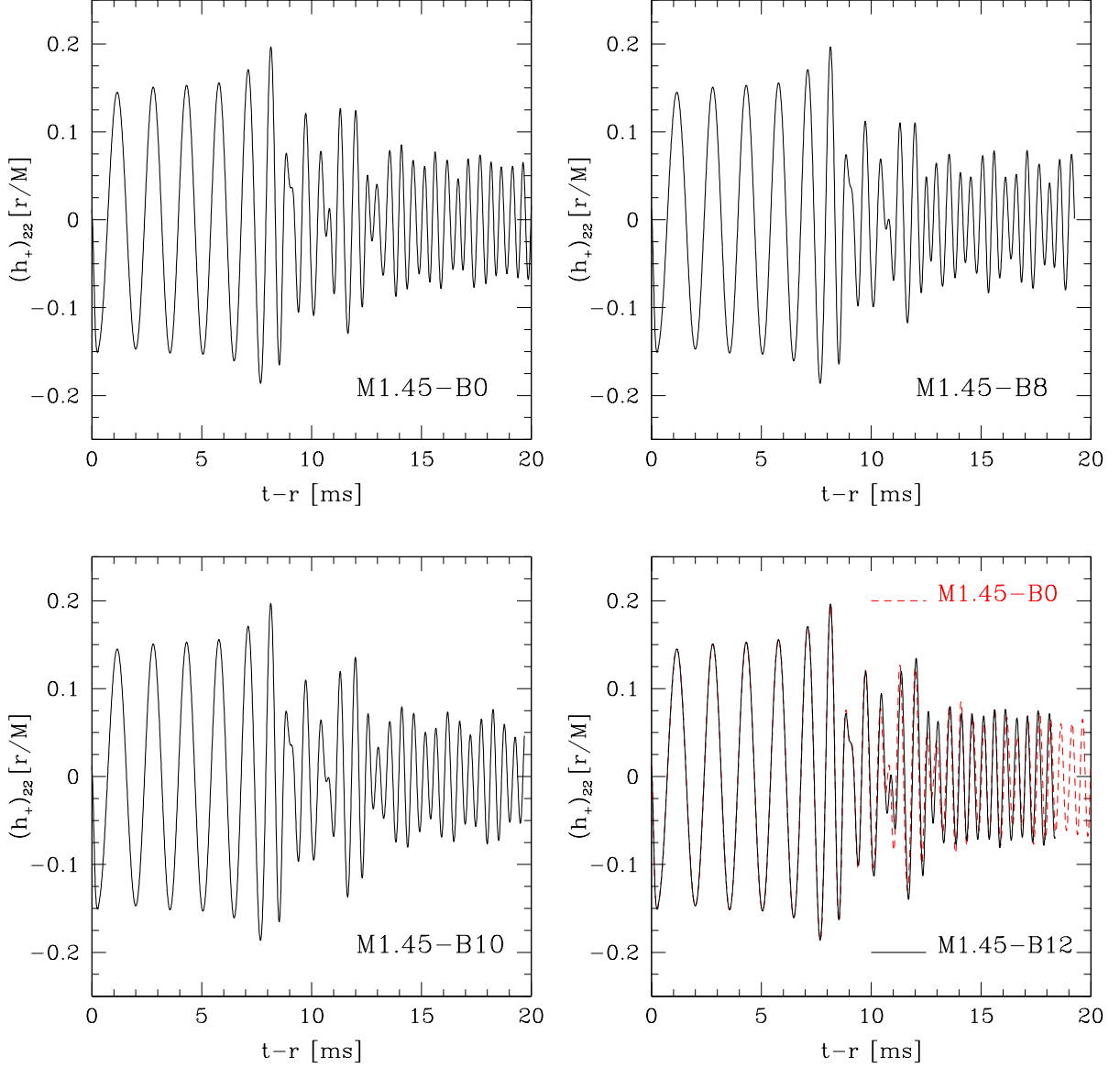
FIG. 9: Gravitational waves for the low-mass binaries as a function of the retarded time $t - r$ in ms. The last panel shows for comparison also the unmagnetized model (*i.e.,* red dashed line which terminates at $t - r = 20$ ms) together with the model `1.45-B12` (black solid line which terminates earlier).

considered as placed at a distance of $100\,\mathrm{Mpc}$. We report also the spectral densities for binaries without magnetic field (solid black line) to aid the comparison. Also shown are the noise curves of the Virgo detector (dotted green line), of the advLIGO [46] and advVirgo [47] detectors (short-dashed blue and dot-dashed magenta lines, respectively), and of the planned Einstein Telescope [15, 48] (dashed red line). With a dotted vertical line we indicate the value of twice the initial orbital frequency f_0, so that the signal for $f < 2f_0$ should be ignored.

In all the panels the part of the signal up to about $700\,\mathrm{Hz}$ is associated with the inspiral part of the waveform and in the case of the high-mass binaries (panels in the left column) it is

also the strongest peak. The low-mass binaries (panels in the right column) also show an additional peak with an amplitude comparable to that at $f \approx 700\,\mathrm{Hz}$ and it is related to (twice) the spinning period of the bar-deformed HMNS. That peak appears for all the models at a frequency of approximately $2\,\mathrm{kHz}$ and its amplitude is sufficiently high to enter into the band of advLIGO.

While we expect the position in frequency of the peak to be accurate, its amplitude clearly depends on the subsequent evolution of the HMNS, which we have followed here only for about $12\,\mathrm{ms}$. Clearly, should the HMNS survive on much longer timescales as shown in [8] (see the right panel of figure A1 in the appendix of [8]), then the amplitude of this peak
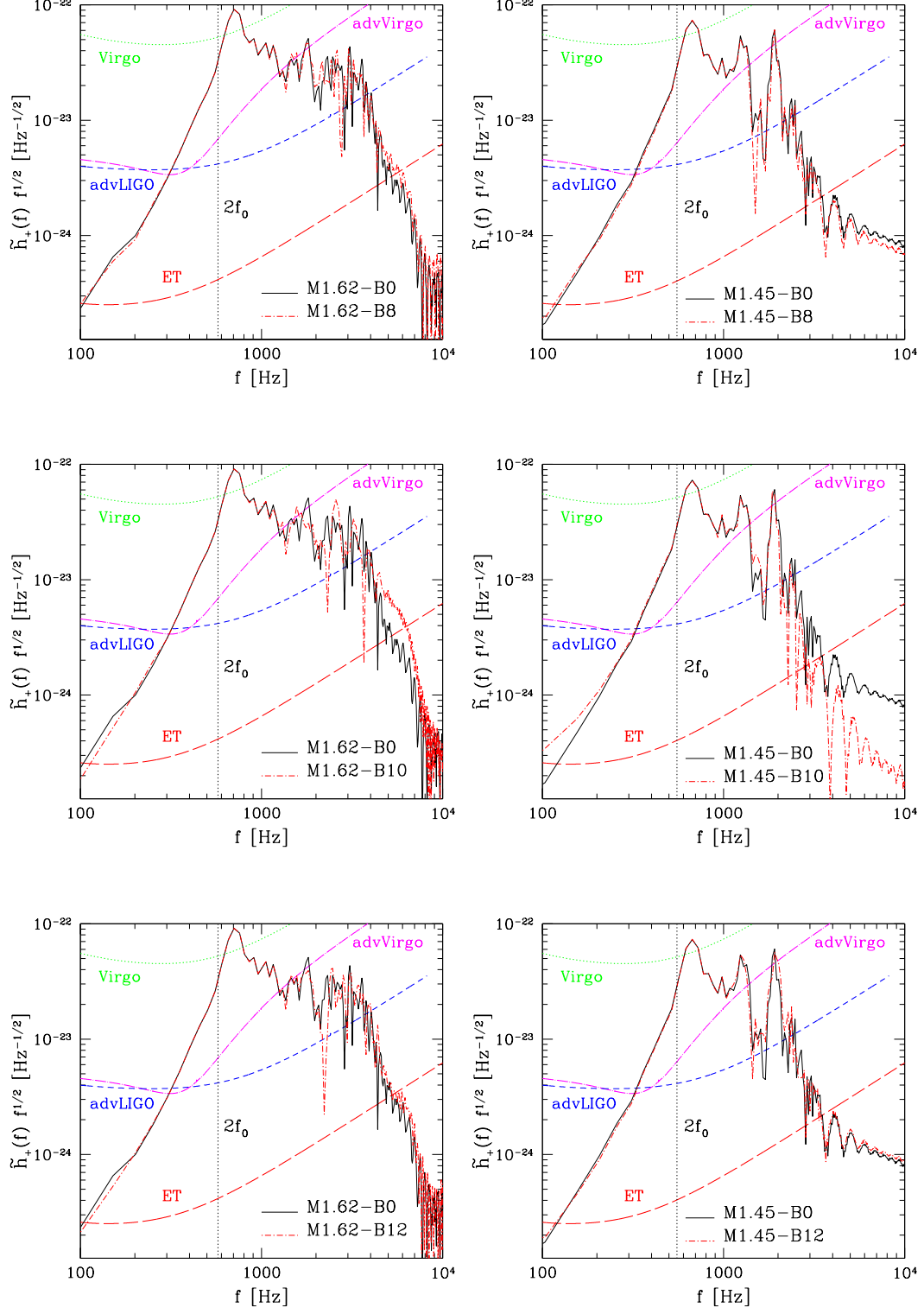
FIG. 10: Scaled power spectral densities $\tilde{h}_+(f)f^{1/2}$ for the high-mass case (left panel) and low-mass case (right panel) without magnetic field (solid black line) or with an initial magnetic field (dot-dashed red line) of $\approx 10^8$ G (first row), $\approx 10^{10}$ G (second row) or $\approx 10^{12}$ G (third row). In all the panels the sources are considered when placed at a distance of 100 Mpc. Shown also are the noise curves of the Virgo detector (dotted green line), of the advanced LIGO and advanced Virgo detectors (short-dashed blue and dot-dashed magenta lines, respectively), and of the planned Einstein Telescope (dashed red line). The dotted vertical line indicates the value of twice the initial orbital frequency f_0.

could be considerably larger and scale with the square root of the period in which the HMNS continues to rotate before collapsing. Even when leaving aside the role that the energy extraction via neutrinos may play on the evolution of the post-merger object, the hydrodynamical survival of the bar deformation in a rapidly rotating star is still a matter of debate. The general-relativistic simulations of isolated NSs first carried out in Ref. [49] and then analyzed in great detail in Ref. [50–52], all indicate that the bar deformation persists only over a timescale which is comparable with (or slightly larger than) the dynamical one[6]. This is due to the coupling between the $m = 2$ bar deformation with other unstable modes (most notably the $m = 1$ one), which grow to comparable amplitudes and suppress the instability, redistributing angular momentum (see also [55] for a perturbative analysis in terms of a Faraday resonance). On the other hand, simulations of stellar-core collapse (see [56] for a recent review and a complete set of references) and the very long simulations carried out in [8] suggest that bar-deformed stellar cores or HMNSs can be produced and survive on timescales much longer than the dynamical one. This different behavior in the persistence of the bar deformation may well be due to the very different distribution of angular momentum and density stratification between the two configurations. Work is ongoing to confirm whether this is actually the case.

Also quite evident from all the panels is that the spectra are very similar but not identical and that these differences become more appreciable for larger initial magnetic fields. Indeed the largest differences appear for $B \simeq 10^{10}$ and, as for the accelerated collapse discussed in Fig. 5, magnetic fields of this strength are those that most influence the postmerger dynamics. Once again, it is worth emphasizing that the spectra presented here refer to a possibly too short portion of the evolution of the HMNS and if the HMNS does survive on much longer timescales, then the small differences shown here would become considerably more pronounced and well within the sensitivities of advanced detectors.

In order to asses in a more quantitative way the possibility to detect these small differences in the GWs, we have computed the overlap between two waveforms $h_{\rm B1},\ h_{\rm B2}$ from binaries with initial magnetic fields B1, B2 as

$$\mathcal{O}[h_{\rm B1}, h_{\rm B2}] \equiv \frac{\langle h_{\rm B1} | h_{\rm B2} \rangle}{\sqrt{\langle h_{\rm B1} | h_{\rm B1} \rangle \langle h_{\rm B2} | h_{\rm B2} \rangle}} , \qquad (16)$$

where $\langle h_{\rm B1} | h_{\rm B2} \rangle$ is the scalar product and is defined as

$$\langle h_{\rm B1} | h_{\rm B2} \rangle \equiv 4 \Re \int_0^\infty df \frac{\tilde{h}_{\rm B1}(f) \tilde{h}^*_{\rm B2}(f)}{S_h(f)} , \qquad (17)$$

and $\tilde{h}(f)$ is the Fourier transform of the GW $h(t)$ and $S_h(f)$ is the noise power spectral density of the detector (we have here considered advLIGO). Taken two waveforms, the closer to 1

is their overlap, the harder will be for a detector to distinguish them.

The overlaps computed for all the magnetized binaries considered here when compared with the corresponding non-magnetized models are collected in Table III. Note that we present both the total overlap $\mathcal{O}$, *i.e.,* the overlap computed over the full time-series, and the overlaps computed over the inspiral only or the post-merger only, *i.e.,* $\mathcal{O}_{\rm insp}$ and $\mathcal{O}_{\rm postm}$, respectively. Given the values in Table III and since present and advanced detectors could potentially distinguish two signals if $\mathcal{O} < 0.995$, it is clear that a detector such as advLIGO or advVirgo would not be able to distinguish between a magnetized binary and an unmagnetized one (*cf.* second column in the Table). Similar considerations apply also when the overlap is computed only over the inspiral phase (*cf.* third column in the Table). However, if the overlap is computed only over the post-merger phase (*cf.* fourth column in the Table) then it is evident that the differences among the various binaries are much larger and the corresponding overlaps considerably smaller. Hence, we conclude that a long-lived HMNS and a detector with sufficient sensitivity at high frequencies (such as the Einstein Telescope) could be able to measure the level of magnetization in the progenitor NSs.

To complete the information about the GW emission from magnetized BNSs, we have also computed the signal-to-noise-ratio (SNR) defined as

$$\left(\frac{S}{N} \right)^2 = 4 \int_0^\infty \frac{|\tilde{h}_+(f)|^2}{S_h(f)} df , \qquad (18)$$

for different detectors and we have listed their values in Table III for a source at $100\,{\rm Mpc}$. Overall, it is easy to realize that while the current Virgo and LIGO detectors (respectively the fifth and sixth columns) would not be able to detect these signals, SNRs larger than 1 are obtained when considering advLIGO and advVirgo, and even larger than 40 in the case of the Einstein Telescope (last column in the Table). It is worth stressing that these SNRs should be seen as lower limits. Firstly, because the binaries are expected to enter the sensitivity band at lower frequencies than the ones considered here, hence adding considerable power to the SNR. Secondly, as discussed extensively above, the possibility of a long-lived HMNS could significantly add to the power at high frequencies, hence increasing the SNR.

In summary: the results presented here indicate that BNSs do represent strong sources of GWs and that these can be detected at distances up to $100\,{\rm Mpc}$ by the planned advanced interferometers. Determining the level of magnetization of the progenitor stars will be very difficult if the detected signal is confined essentially to the inspiral, while it could be possible if the HMNS survives for sufficiently long times as a deformed and spinning bar. In this latter case, detectors which have high sensitivities at high frequencies, such as advLIGO and more importantly the Einstein Telescope, will be in a good position to measure the strength of the magnetic fields and hence extract important physical and astrophysical information on the progenitor NSs.

---

[6] Similar results have been found also in Newtonian simulations [53] and also for magnetized stars [54]

TABLE III: GW-related quantities. Column 2 shows the total overlap computed for advLIGO between the magnetized models and the corresponding unmagnetized binary, while columns 3 and 4 represent the overlap computed over the inspiral and over the post-merger phase. Finally, columns $5-9$ show the SNR computed for different detectors for all the eight models considered here. The SNR has been obtained assuming a source at $100\,\mathrm{Mpc}$.

Binary	$\mathcal{O}$	$\mathcal{O}_{\mathrm{insp}}$	$\mathcal{O}_{\mathrm{postm}}$	SNR (Virgo)	SNR (LIGO)	SNR (AdvVirgo)	SNR (AdvLIGO)	SNR (ET)
M1.45-B0	1.000	1.000	1.000	0.33	0.23	1.94	2.11	38.90
M1.45-B8	0.997	0.999	0.926	0.33	0.23	1.94	2.10	38.72
M1.45-B10	0.996	0.999	0.934	0.33	0.23	1.94	2.11	38.82
M1.45-B12	0.996	0.999	0.899	0.33	0.23	1.94	2.11	39.01
M1.62-B0	1.000	1.000	1.000	0.36	0.25	2.00	2.24	42.57
M1.62-B8	0.998	1.000	0.938	0.36	0.25	2.00	2.24	42.59
M1.62-B10	0.993	1.000	0.724	0.36	0.25	2.00	2.23	42.48
M1.62-B12	0.997	1.000	0.893	0.36	0.25	2.00	2.24	42.49

V. CONCLUSIONS

There is little doubt that BNSs represent prime sources for present and advanced GW detectors. Equally clear is that NSs are observed to have large magnetic fields, with values which can be as high as 10^{16} G for isolated and young magnetars. It is therefore of great importance to assess what is the role that magnetic fields play during the inspiral and merger on BNSs. Extending a research presented in [6], we have presented the first numerical simulations of magnetized BNSs with astrophysically realistic magnetic fields. More specifically, we have carried out a systematic investigation of the dynamics of both matter and magnetic fields of equal-mass BNSs. While previous works [3, 5, 6] considered only astrophysically unrealistic magnetic fields ($B \approx 10^{16} - 10^{17}$ G) or focused mainly on the inspiral part [6], we have here considered magnetic-field values ranging from 10^8 to 10^{12} G, and evolved BNSs through all the stages of the inspiral, merger, HMNS evolution, and collapse to BH.

Overall, we have shown that realistic magnetic fields do not affect sensibly the dynamics of the inspiral, but they can influence that of the post-merger, where they can accelerate the collapse of the HMNS. The different time intervals from the merger to the collapse of the HMNS also imply that the tori produced around the BH have slightly different masses, reflecting the different distributions of matter and angular momentum at the time of collapse. As a result of the tight correlation between the degree of magnetization of the NS matter and the delay time of the collapse, the measurement of the latter via a GW detection will allow to infer the former. To the best of our knowledge, this is the first time that effects of this type have been discussed in the evolution of inspiralling and magnetized NSs.

Magnetic fields can be amplified at the merger of the binary, when a Kelvin-Helmholtz instability develops between the outer layers of the two stars. Although the resolution used here is the highest employed so far in simulating magnetized BNSs and it is sufficient to reveal the development of the instability and the exponential growth of the toroidal magnetic field, the amplification we have measured is only of about one order of magnitude and much smaller than that reported in Ref. [40], where the newly produced fields reach values in equipartition with the kinetic energy. Although it is possible that the different results are due to the different numerical methods employed in Ref. [40], we believe the reason behind our modest amplifications to be that the shear layer between the two stars survives only for about 1 ms, before being destroyed by the collision between the two stellar cores. Such a short timescale and the relatively small velocities at the shear layer are probably insufficient to yield the type of amplification that has been obtained in more "controlled" simulations of the Kelvin-Helmholtz instability [41, 42].

The toroidal magnetic field continues to be amplified also after the Kelvin-Helmholtz instability has been suppressed and it can reach values that are comparable with the initial poloidal one either during the evolution of the HMNS (in the case of low-mass binaries) or during the evolution of the torus produced after the HMNS collapse (in the case of high-mass binaries). This result is particularly important since it suggests that the magnetic field topology in the tori formed from BNS mergers is not purely poloidal, as instead several magnetized accretion disk simulations have assumed so far.

When considered in terms of their GW emission, the magnetized binaries studied here show that it is unlikely that the degree of magnetization will be measurable by present and advanced detectors if the inspiral is the only part of the signal available. However, if the HMNS survives for sufficiently long times as a deformed and spinning bar, then the modifications introduced by the presence of magnetic fields could lead to waveforms which differ appreciably from those of non-magnetized binaries. In this case, detectors which have high sensitivities at frequencies larger than about 2 kHz, such as advLIGO and, more importantly, the Einstein Telescope, will be able to measure these effects for binaries up to distances of about $100\,\mathrm{Mpc}$.

[1] M. Anderson et al., Phys. Rev. D **77**, 024006 (2008).
[2] L. Baiotti, B. Giacomazzo, and L. Rezzolla, Phys. Rev. D **78**, 084033 (2008).
[3] M. Anderson, E. W. Hirschmann, L. Lehner, S. L. Liebling, P. M. Motl, D. Neilsen, C. Palenzuela, and J. E. Tohline, Phys. Rev. Lett. **100**, 191101 (2008).
[4] L. Baiotti, B. Giacomazzo, and L. Rezzolla, Class. Quantum Grav. **26**, 114005 (2009).
[5] Y. T. Liu, S. L. Shapiro, Z. B. Etienne, and K. Taniguchi, Phys. Rev. D **78**, 024012 (2008).
[6] B. Giacomazzo, L. Rezzolla, and L. Baiotti, MNRAS **399**, L164 (2009).
[7] K. Kiuchi, Y. Sekiguchi, M. Shibata, and K. Taniguchi, Phys. Rev. D **80**, 064037 (2009).
[8] L. Rezzolla, L. Baiotti, B. Giacomazzo, D. Link, and J.-A. Font, Class. Quantum Grav. **27**, 114105 (2010).
[9] T. Piran, Phys. Rep. **314**, 575 (1999).
[10] K. Belczynski, R. E. Taam, V. Kalogera, F. Rasio, and T. Bulik, Astrophysical Journal **662**, 504 (2007).
[11] N. Andersson, V. Ferrari, D. I. Jones, K. D. Kokkotas, B. Krishnan, J. Read, L. Rezzolla, and B. Zink, arXiv:0912.0384 (2009).
[12] D. R. Lorimer, Living Reviews in Relativity **4** (2001).
[13] V. Urpin, U. Geppert, and D. Konenkov, MNRAS **295**, 907 (1998).
[14] S. Abdolrahimi, ArXiv e-prints (2009).
[15] M. Punturo et al., Class. Quantum Grav. **27**, 084007 (2010).
[16] L. Baiotti, I. Hawke, P. Montero, and L. Rezzolla, in *Computational Astrophysics in Italy: Methods and Tools*, edited by R. Capuzzo-Dolcetta (MSAIt, Trieste, 2003), vol. 1, p. 210.
[17] L. Baiotti, I. Hawke, P. J. Montero, F. Löffler, L. Rezzolla, N. Stergioulas, J. A. Font, and E. Seidel, Phys. Rev. D **71**, 024035 (2005).
[18] B. Giacomazzo and L. Rezzolla, Class. Quantum Grav. **24**, S235 (2007).
[19] D. Pollney, C. Reisswig, L. Rezzolla, B. Szilágyi, M. Ansorg, B. Deris, P. Diener, E. N. Dorband, M. Koppitz, A. Nagar, et al., Phys. Rev. D **76**, 124002 (2007).
[20] J. Thornburg, Class. Quantum Grav. **21**, 743 (2004).
[21] L. Antón, O. Zanotti, J. A. Miralles, J. M. Martí, J. M. Ibáñez, J. A. Font, and J. A. Pons, Astrophys. J. **637**, 296 (2006).
[22] A. Harten, B. Engquist, S. Osher, and S. R. Chakrabarty, J. Comput. Phys. **71**, 231 (1987).
[23] P. Colella and P. R. Woodward, J. Comput. Phys. **54**, 174 (1984).
[24] A. Harten, P. D. Lax, and B. van Leer, SIAM Rev. **25**, 35 (1983).
[25] G. Toth, J. Comput. Phys. **161**, 605 (2000).
[26] Z. B. Etienne, Y. T. Liu, and S. L. Shapiro (2010).
[27] H. O. Kreiss and J. Oliger, *Methods for the approximate solution of time dependent problems* (GARP publication series No. 10, Geneva, 1973).
[28] J. A. Rossmanith, SIAM J. Sci. Comput. **28**, 1766 (2006).
[29] B. Giacomazzo and L. Rezzolla, Journal of Fluid Mechanics **562**, 223 (2006).
[30] E. Schnetter, S. H. Hawley, and I. Hawke, Class. Quantum Grav. **21**, 1465 (2004).
[31] K. Taniguchi and E. Gourgoulhon, Phys. Rev. D **66**, 104019 (2002).
[32] URL `http://www.lorene.obspm.fr`.
[33] S. A. Teukolsky, Astrophys. J. **185**, 635 (1973).
[34] A. M. Abrahams, L. Rezzolla, M. E. Rupright, A. Anderson, P. Anninos, T. W. Baumgarte, N. T. Bishop, S. R. Brandt, J. C. Browne, K. Camarda, et al., Phys. Rev. Lett. **80**, 1812 (1998).
[35] M. E. Rupright, A. M. Abrahams, and L. Rezzolla, Phys. Rev. D **58**, 044005 (1998).
[36] L. Rezzolla, A. M. Abrahams, R. A. Matzner, M. E. Rupright, and S. L. Shapiro, Phys. Rev. D **59**, 064001 (1999).
[37] V. Moncrief, Annals of Physics **88**, 323 (1974).
[38] A. M. Abrahams and R. H. Price, Phys. Rev. D **53**, 1963 (1996).
[39] A. Nagar and L. Rezzolla, Class. Quantum Grav. **22**, R167 (2005), erratum-ibid. **23**, 4297, (2006).
[40] R. H. Price and S. Rosswog, Science **312**, 719 (2006).
[41] M. Obergaulinger, M. A. Aloy, and E. Müller, Astronomy and Astrophysics **515**, A30 (2010).
[42] W. Zhang, A. MacFadyen, and P. Wang, Astrophys. Journ. Lett. **692**, L40 (2009).
[43] M. D. Duez, Y. T. Liu, S. L. Shapiro, M. Shibata, and B. C. Stephens, Phys. Rev. Lett. **96**, 031101 (2006).
[44] B. C. Stephens, M. D. Duez, Y. T. Liu, S. L. Shapiro, and M. Shibata, Class. Quant. Grav. **24**, S207 (2007).
[45] L. Baiotti and L. Rezzolla, Phys. Rev. Lett. **97**, 141101 (2006).
[46] J. R. Smith and LIGO Scientific Collaboration, Class. Quantum Grav. **26**, 114013 (2009).
[47] Virgo Collaboration, Advanced Virgo Baseline Design, Virgo internal report VIR-0027A-09 (2009).
[48] Einstein Telescope, URL `http://www.et-gw.eu`.
[49] M. Shibata, T. W. Baumgarte, and S. L. Shapiro, Astrophys. J. **542**, 453 (2000).
[50] L. Baiotti, R. De Pietri, G. M. Manca, and L. Rezzolla, Phys. Rev. D. **75**, 044023 (2007).
[51] G. M. Manca, L. Baiotti, R. D. Pietri, and L. Rezzolla, Class. Quantum Grav. **24**, S171 (2007).
[52] G. Corvino, L. Rezzolla, S. Bernuzzi, R. De Pietri, and B. Giacomazzo, Classical and Quantum Gravity **27**, 114104 (2010).
[53] K. C. B. New, J. M. Centrella, and J. E. Tohline, Phys. Rev. D **62**, 064019 (2000).
[54] K. D. Camarda, P. Anninos, P. C. Fragile, and J. A. Font, Astrophys. J. **707**, 1610 (2009).
[55] M. Saijo and Y. Kojima, Phys. Rev. D **77**, 063002 (2008).
[56] C. D. Ott, Classical and Quantum Gravity **26**, 063001 (2009).